Short Term Scientific Mission Report

Sun-induced fluorescence and spectral reflectance for carbon flux modeling in a savanna ecosystem

Javier Pacheco-Labrador, PhD student
Environmental Remote Sensing and Spectroscopy Laboratory (SpecLab), CCHS-CSIC.

HOST: Dr. Micol Rossini. Remote Sensing of Environmental Dynamics Laboratory, DISAT, University of Milano-Bicocca, Milano (IT)
Dates: 12/01/2014 – 20/12/2014

INDEX

Purpose of the STMS

The presented Short Term Scientific Mission (STSM) is focused on the estimation of carbon fluxes in a Mediterranean heterogeneous ecosystem using high spectral and spatial resolution airborne data. The main objective of the STSM was the estimation of Sun Induced Fluorescence (SIF) from the spectral dataset; only available at a sub-optimal spectral resolution. This variable would be later used as a predictor of carbon fluxes -together with other spectral vegetation indices-, in different models. Moreover, the high spatial resolution would allow taking into account the ecosystem heterogeneity, and evaluate its impact on flux models.

The selected study site is a “dehesa” ecosystem; this is a Mediterranean savanna composed by grassland and scattered trees, mainly *Quercus ilex*. In the site, biospheric fluxes are measured using Eddy Covariance method (Baldocchi 2003). An EC tower operates since 2003 and two additional towers were installed in 2014. Imagery was acquired with the Compact Airborne Spectrographic Imager (CASI 1500i) and the Airborne Hyperspectral Scanner (AHS) sensors between 2010 and 2014 in the context of the BIOSPEC (http://www.lineas.cchs.csic.es/biospec) and the FLUXPEC projects (http://www.lineas.cchs.csic.es/fluxpec). Though Gross Primary Production (GPP) and Net Ecosystem Exchange (NEE) have been already estimated via remote sensing, the spatial heterogeneity of ecosystems is still an issue. Difficulty can increase in areas like the selected study site, where vegetation strata with different phenology and physiology can be found Therefore, in this STSM we have used high spatial resolution data to take into account this heterogeneity and evaluate its impact on carbon flux modeling.

Remote sensing-based models used for the estimation of carbon fluxes typically use vegetation indices derived from spectral reflectance, that provide information related with the structure, phenology or physiology of vegetation (Gamon et al. 2006). Moreover, in the last years, vegetation sun-induced fluorescence has been used in the estimation of carbon fluxes (Meroni et al. 2009). This signal provides information about the status of the photosynthetic apparatus of vegetation, and might be also related with the fraction of Absorbed Photosynthetically Active Radiation (fAPAR) (Rossini et al. 2010). However, SIF is a weak signal, and its retrieval is difficult. Though different methods have been described, the spectral features of the CASI camera could be suitable for the use of multispectral radiance-based methods (Meroni et al. 2009). (Panigada et al. 2014) recently reported the use of the Fraunhofer Line Depth Method (FLD) (Maier et al. 2002) to estimate SIF from airborne data and discriminate crop fields under different regimens of stress. Therefore, in this STSM we have proposed explore the retrieval of SIF using multispectral radiance-based methods with the CASI spectral dataset.

Vegetation indices and SIF would be later used to estimate Gross Primary Production (GPP) and Net Ecosystem Exchange (NEE) using different models as proposed in (Rossini et al. 2012). Pure pixels of the different vegetation types -grassland and trees-, would be selected within the footprint of the EC towers and used in models together and separately. These models would be analyzed to understand the relationships existing between the optical signals of each vegetation type and carbon fluxes.

Description of the work carried out during the STMS

1. *PRELIMINARY PROCESSING*

Prior to the start of the STSM, seven CASI images from the available dataset were selected. Sensor radiance and Hemispherical-Directional Reflectance Factor (HDRF) images were geocorrected and resampled to 1 m x 1 m pixel using the nearest neighborhood method to avoid the spectral mix of different covers during this process.

The location of each eddy covariance tower and the corresponding footprints selected to extract the optical data are shown in the Figure 1. The tower "Centre" is the oldest, while the towers "North" and "South" were installed in 2014, and therefore are only used this year. The footprints include not only vegetation, but also roads and bare soil produced by a firebreak and the installation of the new towers in 2014 (some of them are not noticeable in the RGB image in Figure 1). Moreover, on the north of the tower "Centre" there are solar panels which number has varied between the different flight campaigns.

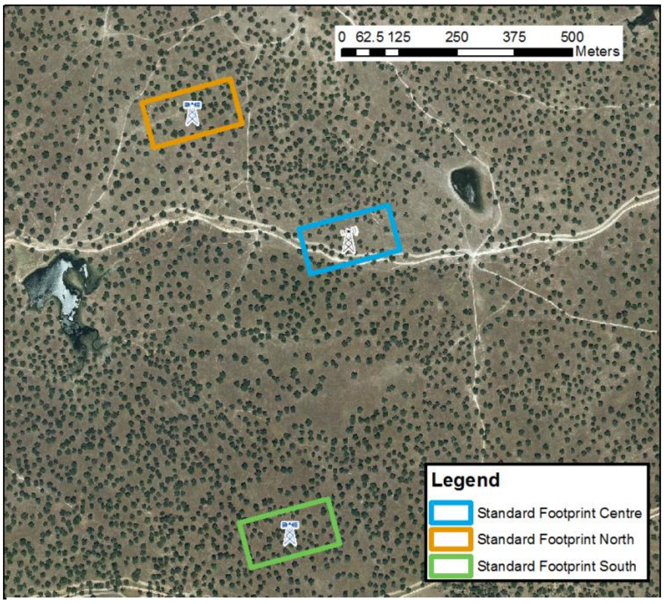

Figure 1. Study site in Las Majadas del Tietar, Cáceres, Spain.

The characteristics and acquisition configuration of the CASI images selected are shown in Table 1. All the images were centered over the eddy covariance tower "Center", but the last two last, which correspond to the towers "North" (P03E2) and "South" (P07E2) installed in the area in 2014. All the images were acquired binning the spectral bands by 2, but the first image acquired in 2010. This image was acquired using the full resolution spectral configuration, presenting 288 bands. Therefore, prior to other analyses it was resampled to 144 bands using the spectral convolution method (Meroni et al. 2010).

Table 1. Features of selected images.

Date	Time	Bands	FWHM (nm)	SSI (nm)	Image Name	Flight Azimuth (degrees)	Solar Azimuth (degrees)
18th May 2010	11:27	288	2.4	~2.40	P11SF	120	170.1
5th May 2011	10:31	144	5.5	~4.75	P01E2am	298	127.2
5th May 2011	14:47	144	5.5	~4.75	P01E2pm	128	244.1
4th Oct 2012	11:13	144	4.8	~4.75	P11E2	181	159.8
8th Apr 2014	11:47	144	5	~4.75	P01E2	192.2	162.9
8th Apr 2014	12:38	144	5	~4.75	P03E2	75	186.14
8th Apr 2014	12:55	144	5	~4.75	P07E2	75	193.61

As shown in the table, acquisition configurations and angles respect to the sun are different for each image, since the targets of the different campaigns carried out in the site were each in each case. Images were selected trying to minimize the differences between the flight and the sun angles, however, this was not always possible, and had to be considered in the later analyses.

Each image was classified in four different categories: grassland, trees, shadows / water and soils/roads using a supervised methodology based on the Mahalanobis Distance method (Richards 1999). Training fields were manually selected in each image. Different spectral indices were computed and used together with the original HDRF bands in the classification.

2. SUN-INDUCED FLUORESCENCE ESTIMATION

For the estimation of SIF, two different methods were selected, FLD and its more sophisticated version, the 3FLD method. These methods are based on atmospheric variables inside and outside a dark line in the irradiance spectrum, most usually the O_2-A absorption band centered at 760.4 nm. The knowledge of incoming irradiance, transmittance and path radiance allow separating the reflected radiance and the fraction corresponding to the fluorescence emission (Maier et al. 2002). In the case of the FLD method, a band inside and another outside of the absorption band are selected whereas in the 3FLD, the radiance outside is interpolated between two bands located at both sides of the dark line. When atmospheric parameters are not available, a variable related with SIF can be empirically estimated from the radiances of non-fluorescent surfaces solving a system where the coefficients estimated are function of these atmospheric parameters, as shown in (Panigada et al. 2014).

Since in our case not atmospheric parameters had been retrieved in a pixel basis, non-fluorescent targets (NFT) were selected in each image in order to use this empirical approach. Different selection criteria were tested, proximity to footprint, proximity to nadir or maximize the range of radiances. The aim was minimize the differences in the atmospheric parameters of these pixels due to spatial variability or observation angle respectively. Pixels were also selected within homogeneous areas, in order to minimize adjacency effects due to pollution of the fluorescent signal from vegetation contiguous vegetation pixels other issues such as spatial cross-talk. We first selected the road and soil pixels found within the footprints; however, these offered a short range of radiances which were usually as bright or brighter than vegetation pixels, but not darker. Nonetheless, the FLD method (Maier et al. 2002) makes recommendable selecting a wide range of non-fluorescent radiances within and outside the atmospheric absorption band, in order to minimize the errors in the fit of the coefficients k_1 and k_2. Therefore, selection was manually done afterwards, looking for bright and very dark pixels (like water surfaces).

Radiances of these NFT pixels were extracted from each image and in order to select the different bands used in the estimation of SIF. The band "inside" the absorption feature was identified as the band with the minimum radiance around 760.4 nm. For the FLD method, the band "outside" the O_2-A band was the one with the maximum radiance at a shorter wavelength than the band "inside" but closer than 12.5 nm. Similarly, a second band "outside" placed at a larger wavelength than the "inside" band was selected for the 3FLD method, also closer than 12.5 nm. For this method, the radiance "outside" was calculated interpolating the radiance of the two "outside" bands to the band "inside". Though different criteria were used to select such targets, the bands selected for the SIF retrieval remained constant. After selecting the bands, radiances were used to adjust the corresponding coefficients k_1 and k_2 for each image solving the system described in (1); where L_{i_n} is the radiance "inside" the O_2-A absorption band in the non-fluorescent pixel and L_{o_n} is the corresponding radiance "outside" the atmospheric feature.

$$\begin{bmatrix} L_{i_1} \\ \vdots \\ L_{i_n} \end{bmatrix} = \begin{bmatrix} L_{o_1} & 1 \\ \vdots & \vdots \\ L_{o_n} & 1 \end{bmatrix} \begin{bmatrix} k_1 \\ k_2 \end{bmatrix} \qquad (1)$$

Afterwards, the coefficients were used to generate "pseudo-fluorescence" (from now on called SIF*) using the radiance "inside" and "outside" of the geocorrected images using the equation (2).

$$L^f k_3 = L_i - L_o\, k_1 - k_2 \qquad (2)$$

Then, estimated SIF* and also reflectance factors were extracted from a standard footprint described as a 100 m x 200 m rectangle centered in each EC tower and oriented in the main wind direction.

The "pseudo-fluorescence" values of the different covers in the footprint were compared. As a result, systematic errors and inconsistencies in the values generated were found. This led to carry out further analyses and try to correct these estimates. A sensor-column-related dependence of the retrievals of florescence was detected. We tried to characterize this effect selecting no-fluorescent targets across the sensor columns in the non-geocorrected images (L1b); and then adjust a function that predicted the coefficients k_1 and k_2 as a function of the column number. Different automatic methods of target selection were tested, based on the radiance and the reflectance of the pixels. Eventually, targets were selected manually in order to have a maximum control of the quality of the pixels selected, located into homogeneous areas both clear and bright. We used these targets to fit the coefficients k_1 and k_2 in each image column solving (1). Moreover, in order to increase the robustness and range of values used to fit the coefficients k_1 and k_2, available NFT were selected within a 50 columns window. In each image, a polynomial was adjusted to predict the value of the coefficients as a function of the column number. Moreover, in order to avoid any likely influence of outliers, a weighted fit was used. Predicted coefficients were then used to estimate fluorescence in each sensor column; these images were later geocorrected. Additionally, we analytically characterized the source of the biases found, and the likely effects that this could have on the fluorescence retrievals of coefficients k_1 and k_2.

3. *SUN-INDUCED FLUORESCENCE AND REMOTE INFORMATION ANALYSIS. MODEL DEFINITION. MODEL CALIBRATION AND ANALYSIS*

Vegetation productivity can be related with optical information as indicators of different vegetation variables (Rossini et al. 2012). On one hand, spectral vegetation indices usually are related with structural parameters of vegetation and/or with the chlorophyll content. These indices relate with GPP since they are linked to the green biomass available to capture radiation photosynthesize (Rossini et al. 2010). In order to estimate GPP and NEE using different models, the following indices were calculated: Normalized Difference Vegetation Index (NDVI), Renormalized Difference Vegetation Index (RDVI), Enhanced Vegetation Index (EVI), Modified Chlorophyll Absorption Ratio Index 1 (MCARI1), Modified Chlorophyll Absorption Ratio Index 2 (MCARI2), Modified Triangular Vegetation Index (MTVI2), Transformed Chlorophyll Absorption Ratio Index/Optimized Soil-Adjusted Vegetation Index (TCARI/OSAVI), Triangular Vegetation Index (TVI), Red-Edge Chlorophyll Index (CIre), Modified Terrestrial Chlorophyll Index (MTCI), and Vogelman Index (VOG).

On the other hand, some spectral indices are related with the Xanthophyll pigments, involved the release of excessive radiation via thermal dissipation. The Photochemical Reflectance Index (Gamon et al. 1992) and derived versions are usually related to the Light Use Efficiency, and therefore with the fraction of the absorbed radiation that is actually used in photosynthesis. PRI and PRI_{515}, -reported less dependent of structural parameters (Hernández-Clemente et al. 2011)- were computed to be included in the GPP/NEE models as LUE estimators. SIF* was computed to be used as a LUE estimator since chlorophyll fluorescence is itself another mechanism of energy dissipation to prevent photodamage. However, inconsistencies in the results found prevented from using SIF* estimates in the models.

Additionally, in some of the models, the Photosynthetic Active Radiation (PAR), continuously measured by the Eddy Covariance systems was included in the models. This variable and also GPP and NEE were aggregated in the temporal domain, intra and inter-daily. This way, flux data representative of different periods of time were compared with the optical data, concretely with the spectral vegetation indices indicators computed.

The models described in (Rossini et al. 2012) were selected to predict carbon fluxes are numbered from 1 to 5 as follows. VI is a vegetation index related to green biomass; only two spectral indices, the PRI and the PRI_{515} were used as LUE indicators:

Model 1: $GPP = a + b \cdot VI$

Model 2: $GPP = a + b \cdot VI \cdot PAR$

Model 3: $GPP = (a + b \cdot VI) \cdot PAR$

Model 4: $GPP = (a + b \cdot VI) \cdot (c + d \cdot PRI) \cdot PAR$

Model 5: $GPP = (a + b \cdot VI) \cdot (c + d \cdot PRI_{515}) \cdot PAR$

Using meteorological data and the optical information extracted from each cover (trees and grassland) within the footprints, the models were adjusted using the non-linear optimization method implemented in the Matlab^{TM} function *lsqcurvefit*. For that we used separately the data from the grass cover and the oak cover; afterwards, these spectral data were linearly mixed based on the proportion of pixels of each category. Eventually, all the spectral data of all the pixels in the footprint, including shadows, water, bare soils, and roads were merged and used to fit each models. Models were fit against instantaneous and daily aggregated GPP and NEE. Results for each model and for each cover were analyzed.

Description of the main results obtained

1. *PRELIMINARY WORKS*

Spatial resolution of the images allowed discriminating the different elements in the scene: grassland, trees, shadows casted by the trees and non-vegetation covers like bare soils, tracks… The fractions of the different cover types in the footprints (one in 2010, 2011 and 2012 and three in 2014) of each image as classified using the supervised classification method are shown in Table 2. Footprints size ranges between 19880 and 20073 pixels. In all the cases, the grassland is the predominant category, followed by the trees; and then by tree-shadows and bare soils and roads indistinctly. However, the last two categories represent more than the 10% of the surface of each footprint.

Table 2. Fraction cover of each classified category in the different footprints.

Image	Grass	Trees	Shadow	Soil and Roads
100518_P11SF	71.94%	16.83%	4.82%	6.41%
110505_P01E2am	71.47%	16.53%	6.96%	5.03%
110505_P01E2pm	67.74%	17.57%	10.40%	4.29%
121004_P11E2	65.89%	15.04%	14.61%	4.46%
140408_P01E2	72.56%	17.07%	7.38%	2.99%
140408_P03E2	67.31%	21.04%	9.15%	2.51%
140408_P07E2	67.22%	21.86%	10.22%	0.70%

2. *SUN-INDUCED FLUORESCENCE ESTIMATION*

Figure 2 shows radiances corresponding to the NFT outside the footprint and to the vegetation types within the footprint. The bands selected for SIF* retrieval are marked with red circles. As can be seen, bright and dark NFT were selected attempting to maximize the range of radiances. However, radiances of some vegetation pixels are still larger than the highest radiances among the NFT in the near infra-red (NIR).

After band selection in each image, SIF* was calculated using both the FLD and 3FLD methods. The first analysis done was comparing the estimates of the different covers of each image. Moreover, SIF* retrievals were plotted against the radiance values outside the atmospheric absorption band (L_o) in order to discard any relationship between both variables. In all the cases and for both methods, we found inconsistencies that lead us to question the results. In some cases, the NFT within the footprint seemed to emit fluorescence, with magnitudes sometimes close to the emission of vegetation targets. This could be partially explained by adjacency effects, since these targets do not form large patches within the footprint, but are most usually linear features, where this effect can importantly operate. On the contrary, this could not justify the cases when this was observed in the NFTs used to estimate the coefficients, as shown in Figure 3. As can be observed, both soils and roads within the footprint and also selected NFTs outside the footprint show positive values of SIF at sensor radiances between 50 and 100 mW/m^2 sr nm. This might suggest a non-linear relationship between the radiance inside and outside the O_2-A band.

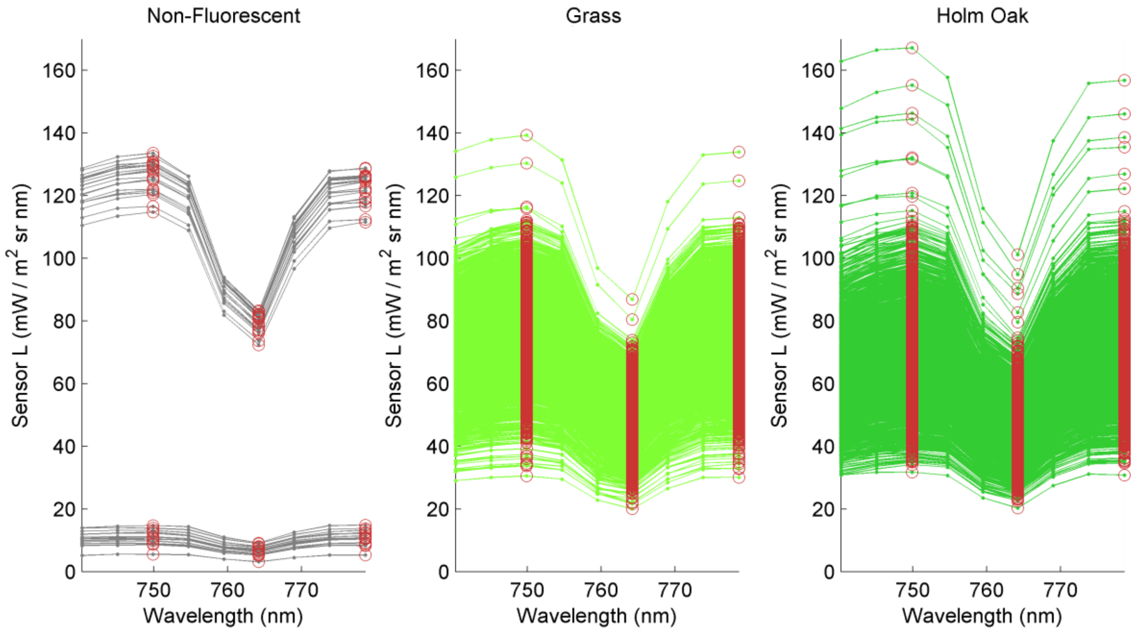

Figure 2. Sensor radiances around the O_2-A band corresponding to the image 140408_P01E2, acquired over the "Centre" tower in April 2014. Non-fluorescent targets were used to select the bands inside and outside the atmospheric feature. Selected bands are signaled with red circles. Moreover, radiances corresponding to the two vegetation types within the footprint are shown on the right; selected bands are also indicated with red circles.

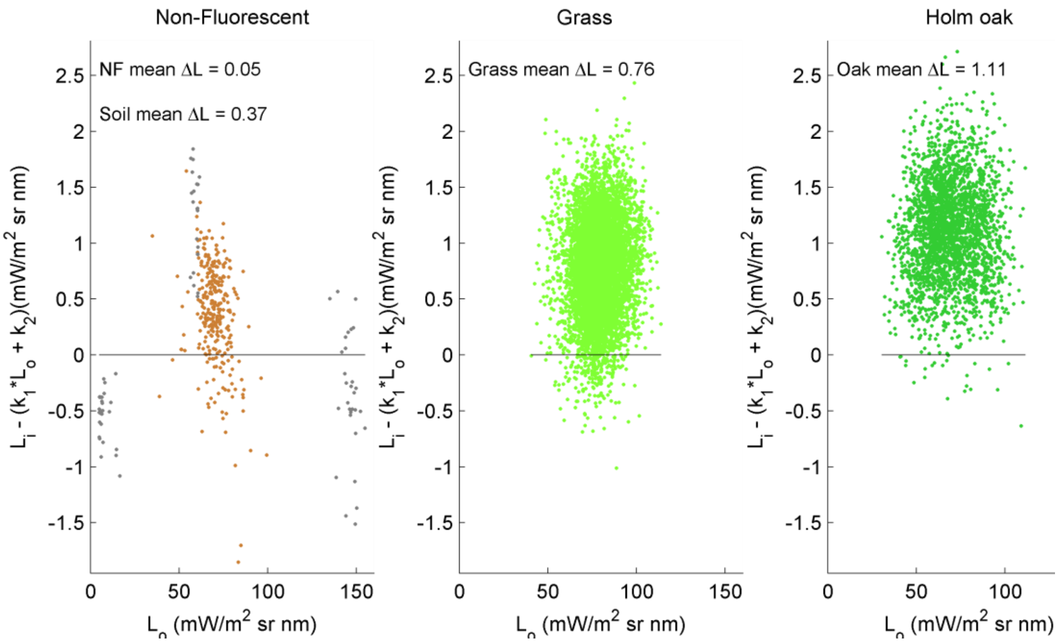

Figure 3. SIF* estimates in the image 140408_P03E2 acquired in April 2014 using the FLD method. In the left graph, grey dots correspond to NFTs selected to adjust the coefficients k_1 and k_2 out of the footprint; whereas brown dots are the soil and road pixels within the footprint of the EC tower. In the center graph, light green points correspond to the grass pixels within the footprint, whereas in the right graph, dark green dots correspond to SIF* estimates of the tree pixels within the footprint.

In other cases, negative values of SIF* were estimated, both in NFTs and in vegetation pixels. This might be explained by differences in the atmospheric parameters found in the pixels used to fit the coefficients and in those where SIF* was later estimated. For this reason we attempted to select pixels close to the footprint and or close to nadir. However, meeting these criteria was never possible in all the scenes. Figure 4, shows an example of this case. The image corresponds to October, when grass was almost completely dry, and therefore low values of SIF* would be expected. However, as can be seen, SIF* values (estimated with the 3FLD method) are negative for soils and roads within the footprint and also for the grass pixels within the footprint. Results obtained by the FLD method are also negative for soils and roads, but not for grassland. Thus, though in some cases, the values estimated for vegetation covers seemed to make sense, the values found in pixels where should be no emission led us to question such estimates.

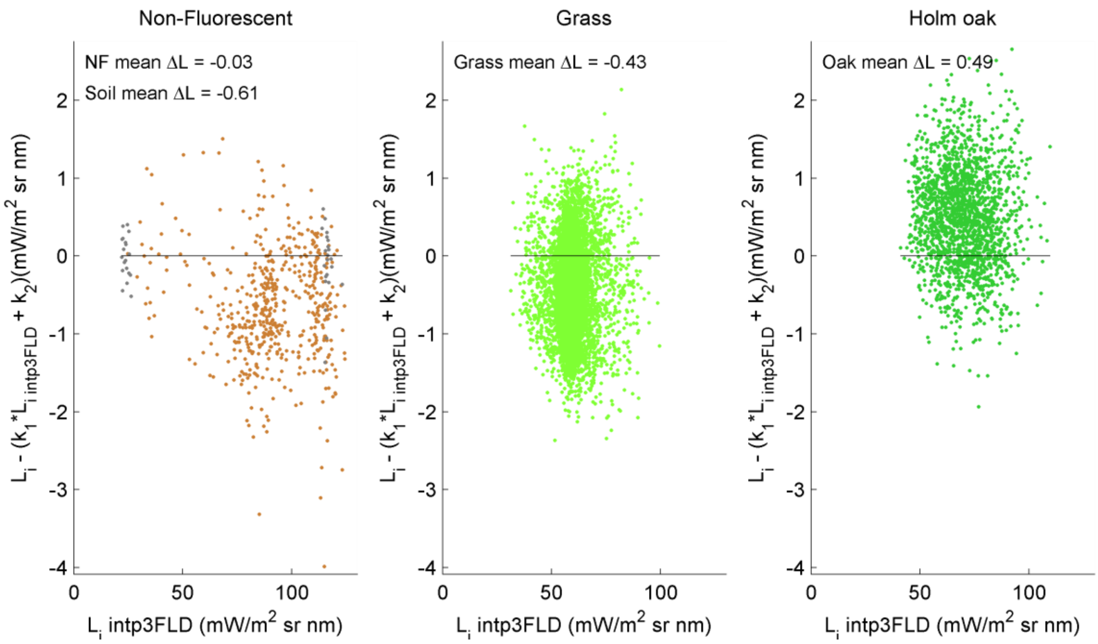

Figure 4. SIF estimates in the image 121004_P11E2 acquired in October 2012 using the 3FLD method. In the left graph, grey dots correspond to NFTs selected to adjust the coefficients k_1 and k_2 out of the footprint; whereas brown dots are the soil and road pixels within the footprint of the EC tower. In the center graph, light green points correspond to the grass pixels within the footprint, whereas in the right graph, dark green dots correspond to SIF estimates of the tree pixels within the footprint.

SIF* estimates were calculated from the radiances extracted from pixel images. In order to better understand the inconsistencies found, fluorescence maps were generated and visualized. SIF* values seemed to gradually increase across-track. We discarded the existence of any directional effect checking that this increase was not related with the sun position, which suggested that this could be a sensor-related problem. SIF* was computed using the original non-geocorrected images, and an increase of values from left to right was found in all the images. This could explain some of the problems previously found, since the NFTs selected were some times in pixels where the magnitudes of this gradient were significantly different. The source of this dependence has not been confirmed, though at this point we suspected that stray light effects could be in part the responsible.

Figure 5 shows an example of the coefficients fit in the image 121004_P11E2. As in all the cases, k_1 increased from left to right in the sensor. The trends in k_2 were not so much consistent, and usually noisy. In fact the magnitude of this noise was important compared with the SIF values latter estimated.

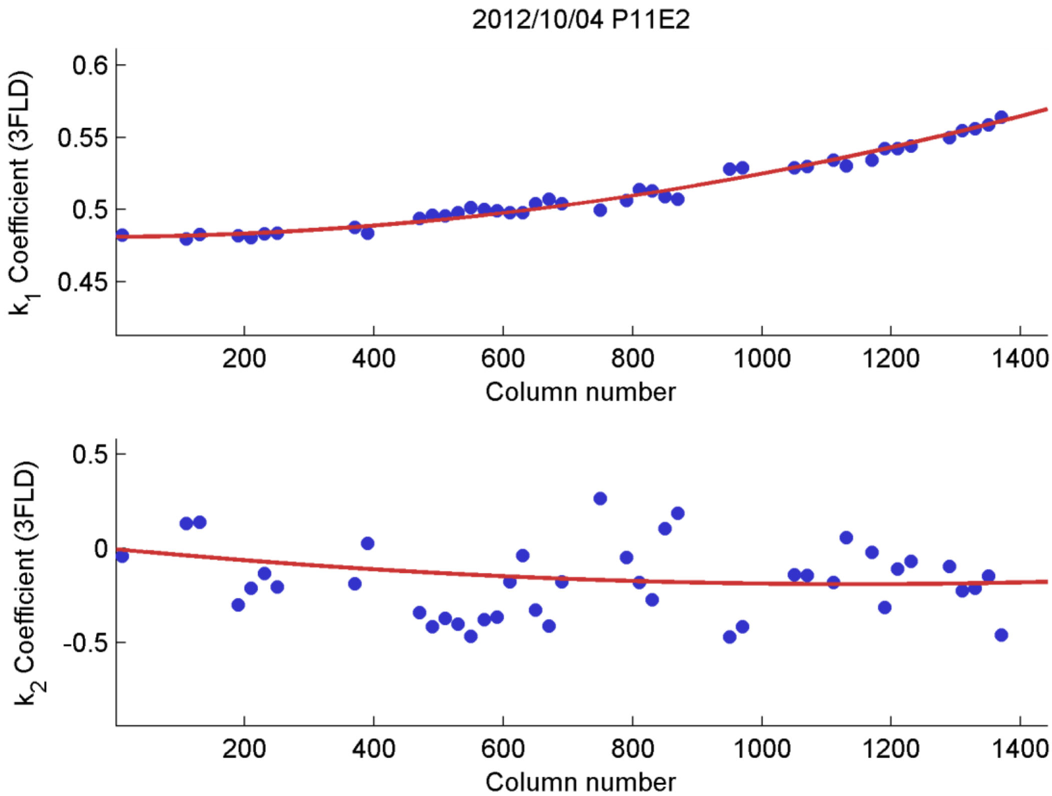

Figure 5. Coefficients k_1 and k_2 measured and estimated across-track corresponding to the image 121004_P11E2 acquired in October 2012. Coefficients are estimated for the 3FLD method. Blue dots correspond to coefficients fit using targets selected in a 50 columns moving window and red lines the corresponding predicted values as a function of the column number using weighted polynomials.

Coefficients predicted as a function of the column number were used to estimate SIF* from the L1b images, these were afterwards geocorrected and pixels in the footprint extracted. This method allowed the removal of the column-dependency previously observed. Figure 6 shows an example of SIF* maps calculated using unique (top) and column dependent coefficients (bottom). In the image of the top there is a clear increase of brightness from left to right, which disappears in the image of the bottom, where the column-based method is applied. This correction enhanced the differences between non-fluorescent targets and vegetation. Despite of the fact that the column-dependencies were apparently removed, the magnitude of SIF* values were still inconsistent, and negative values still appeared in NFT and soils in some of the images. At this point and considering other limitations such as ancillary data available and the duration of the STMS among others, the estimation of reliable SIF* should be discarded. A latter effort was done to better understand the influence of this sensor-dependence effect and in general of any noise in the FLD method. For that, we analytically included a spurious radiance in the equations.

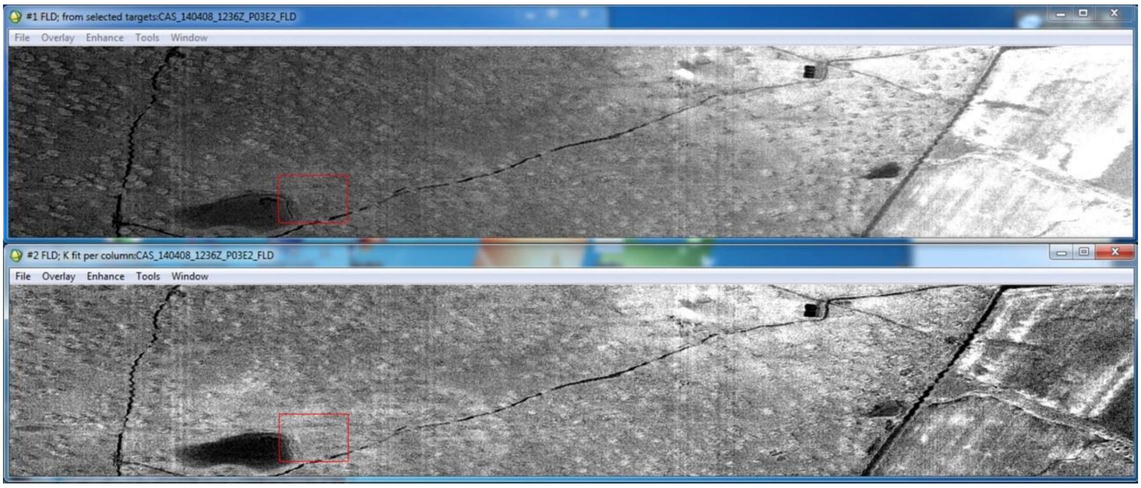

Figure 6. SIF* maps generated from the L1b image 140408_P03E2 acquired in April 2014, using the FLD method. In the top image SIF* is estimated using unique coefficients k_1 and k_2 obtained from targets selected in the geocorrected image. In the bottom image, SIF* is estimated in the non-geocorrected image using coefficients that were function of the column number.

We modeled the at-sensor radiance (L) as (Maier et al. 2002), including a spurious radiance variable which summarizes any likely source of error, not necessarily known, and whose value could be positive or negative, L^s.

$$L = \left(\rho E + L^f\right)T + L^p + L^s \tag{3}$$

where E is irradiance, L^f the fluorescence emission, T the atmospheric transmittance and L^p the path radiance. From here, we rebuilt equation (2) as follows (see appendix I for a complete description):

$$L^f k_3 = L_i - L_o\, k_1 - (k_2 + k_s) = L_i - L_o\, {k_1}^* - {k_2}^* \tag{4}$$

where i stands for inside the O_2-A absorption band and o for outside this band; ks is a coefficient that linearly depends on the spurious radiance as k_2 depends on L^p (5). Morevoer k_1^* and k_2^* would be the coefficients eventually adjusted using radiances from non-fluorescent targets.

$$k_s = {L^s}_i - {L^s}_o\, k_1 \tag{5}$$

We used this model to simulate three different situations, trying to understand when would be actually possible retrieving SIF*. The Case 1 is that L^s is 0. The Case 2 is that can be accepted that L^s inside and outside the O_2-A band is constant for all the targets. Finally the Case 3 is that L^s inside and outside the O_2-A band is different for each target, no matter whether it is equal or different inside or outside the band of each target. Figure 7 shows the result of the simulation. The blue symbols and line represent Case 1, when there is no spurious radiance and the estimated coefficients are equal to real: $k_1^* = k_1$ and $k_2^* = k_2$. The green symbols and line represent the Case 2, if L^s is equivalent for all the targets and bands, then the offset of the regression would be biased, $k_2^* \neq k_2$, but not the slope $k_1^* = k_1$. Red circles show Case 3, where L^s is different for the each target, none of the estimated coefficients can be equal to the real ones. This happens no matter whether this spurious signal is equivalent inside and outside the O_2-A band. The only exception would occur when for all the targets, the ratio $L_i^s / L_o^s = k_1$. In that case, the coefficients estimated would be the same that the real ones since k_s would cancel out as shown in equation (5). Case 3 might also produce a non-linear relationship between the radiances inside and outside the absorption feature, if L^s was related to L_i or/and L_o; which would make the SIF* estimates dependent on the radiance of the NFT selected for the retrieval of k_1 and k_2, and also inconsistencies in the retrieval of SIF*.

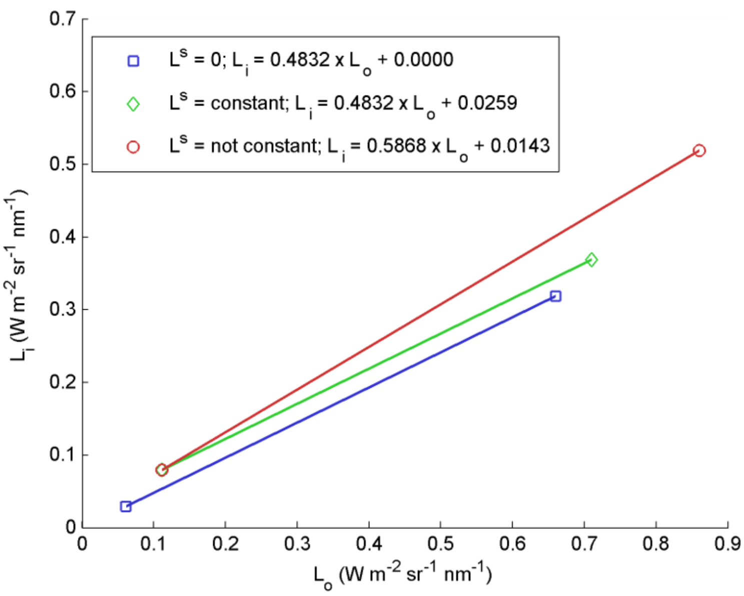

Figure 7. Simulation of the retrieval of coefficients k_1 and k_2 under different types of L^s.

Since in all the cases the coefficient k_1 showed a dependence on the column number, we deduced that, in our imagery, spurious radiance was different or lead to an effect of different magnitude also for the different bright and dark NFT selected to adjust the coefficients. Thought we originally suspected that stray-light might be responsible of the dependencies found in the SIF* images, it would likely produced a Case 2 situation (same L^s for bright and dark targets, but different in each column). However, in this case, it is the difference between L^s of bright and dark targets what seems to be changing across-sensor. A deeper analysis of the sources of this effect and their mechanisms is out of the scope of this STMS. Moreover, it must be considered that also other factors might operate simultaneously, like differences in the atmospheric parameters within the image that were not characterized; instrumental dependencies related with the radiance level of the targets, such as spectral cross-talk or non-linearities or directional effects; spectral shifts and changes in the spectral resolution across-track; or directional effects among others. A robust analysis of the impact of this spurious radiance on the retrieval of SIF* would be also out of reach of this STMS. However, a preliminary analysis suggested that this could lead also to negative values and explain some of the inconsistencies found, preventing from using these estimates in a multi-temporal or a multi-image analysis.

3. *SUN-INDUCED FLUORESCENCE AND REMOTE INFORMATION ANALYSIS. MODEL DEFINITION. MODEL CALIBRATION AND ANALYSIS*

Figure 8 summarizes some of the spectral and flux data available for the modeling.

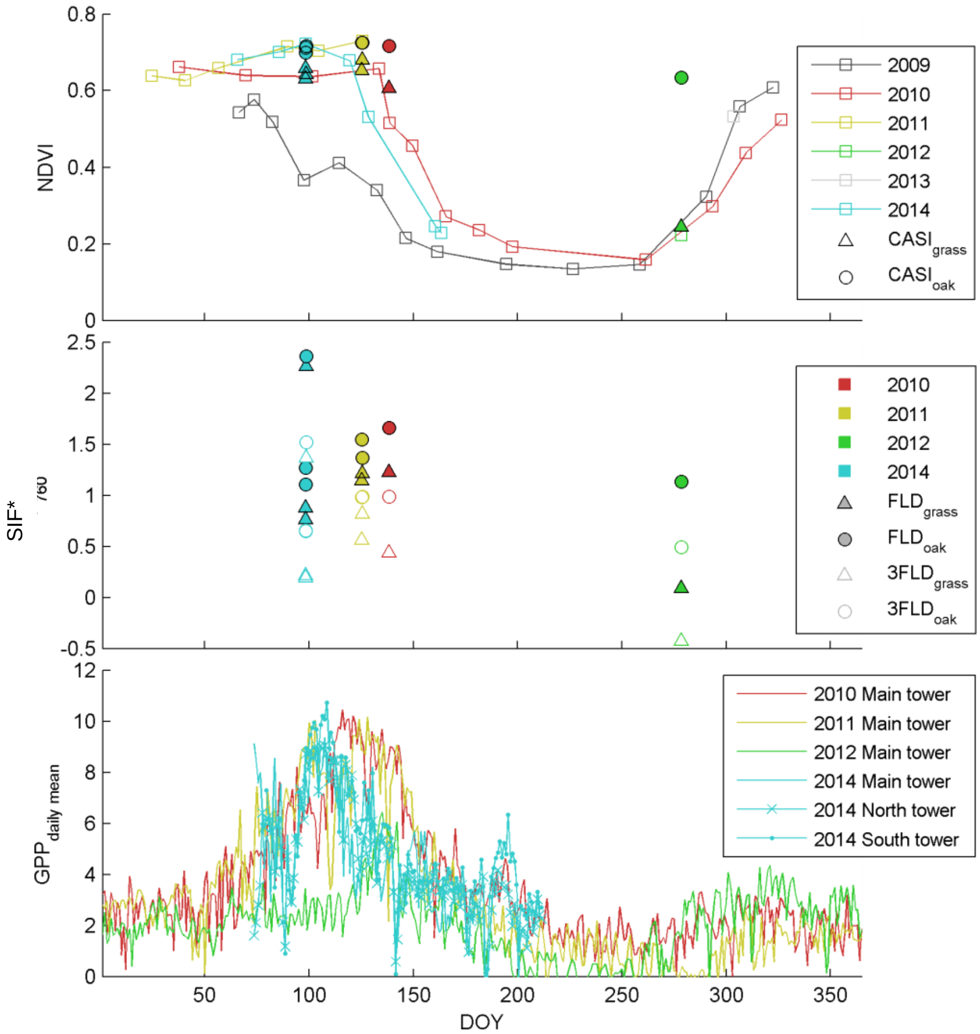

Figure 8. Summary of spectral and eddy covariance datasets available for modeling. On the top graph, ground and airborne derived NDVI, squares stand for grassland and circles for trees. In the middle graph the plot shows, SIF* estimates using both FLD and 3FLD methods. In the bottom graph, daily mean GPP of each tower and year are plotted.

The top graph in figure 8 allows comparing the NDVI calculated from the airborne imagery with ground spectral measurements over grass plots acquired with an ASD Fieldspec® 3 during the field campaigns supported by BIOSPEC and FLUXPEC projects. High agreement can be observed between ground and airborne measurements. In the middle plot in figure 8, the last estimates of SIF* using both FLD and 3FLD methods are shown. Some trends can be seen, somehow related with carbon fluxes. However, as discussed in the previous section, these estimates might be modified by instrumental effects, and would not be used in the modeling. The bottom graph in figure 8 shows the daily mean GPP. As can be seen, there are some significant differences between years.

As previously mentioned, a set of spectral indices were calculated from the spectral reflectance extracted from the classified footprints. Averages for each cover were calculated, and the relationships existing among them for both, grass and trees, was investigated. Figure 9 shows the indices scatterplot matrix corresponding to grass pixels. As can be seen, most of the indices are highly correlated among them except for the MTCI and the PRI and PRI_{515} indices.

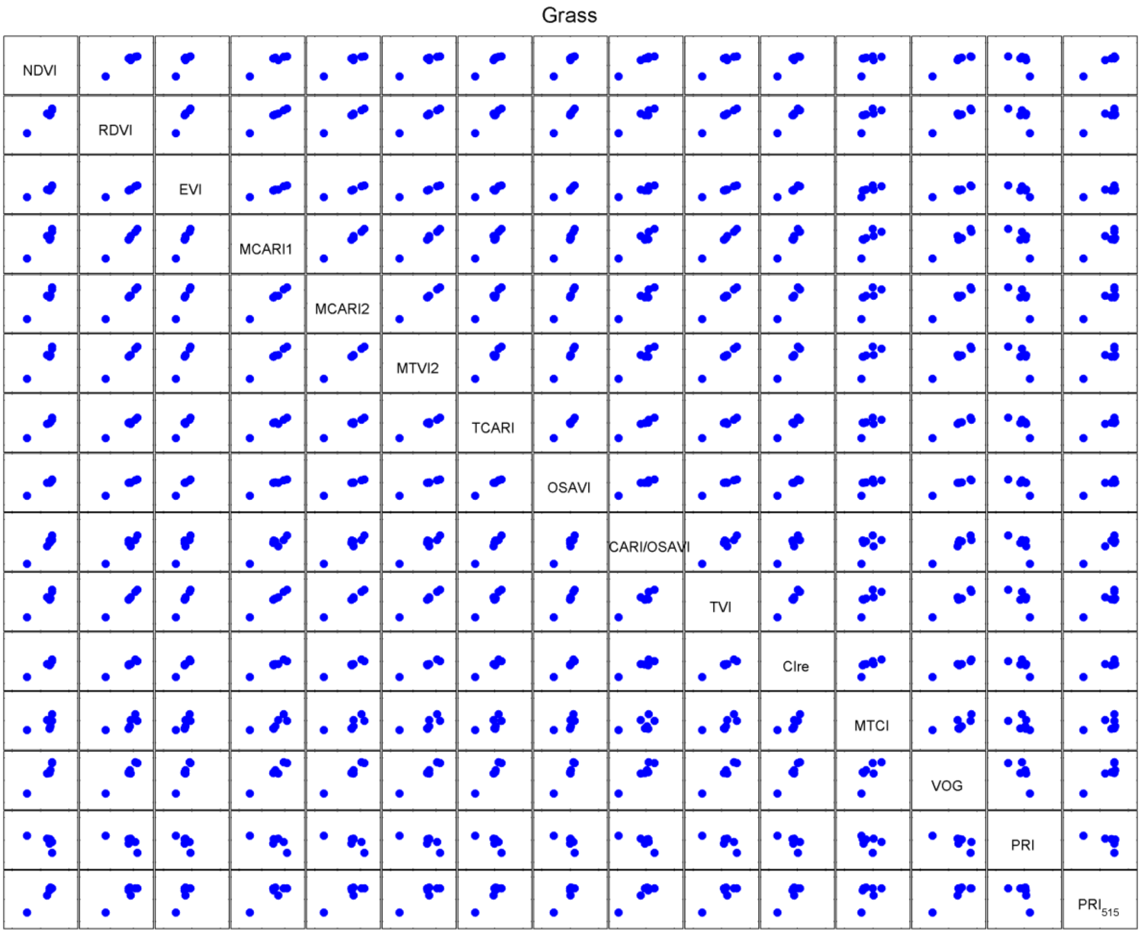

Figure 9. Scatter plots matrix between the different spectral indices obtained from grass pixels reflectance.

In the case of the indices calculated from tree pixels (Figure 10), high correlation values are not so frequently found. Some indices such as MCARI1, TCARI, TCARI/OSAVI… show almost no correlation with the rest of the indices. In these cases, PRI indices did not show clear relationship with any other indices.

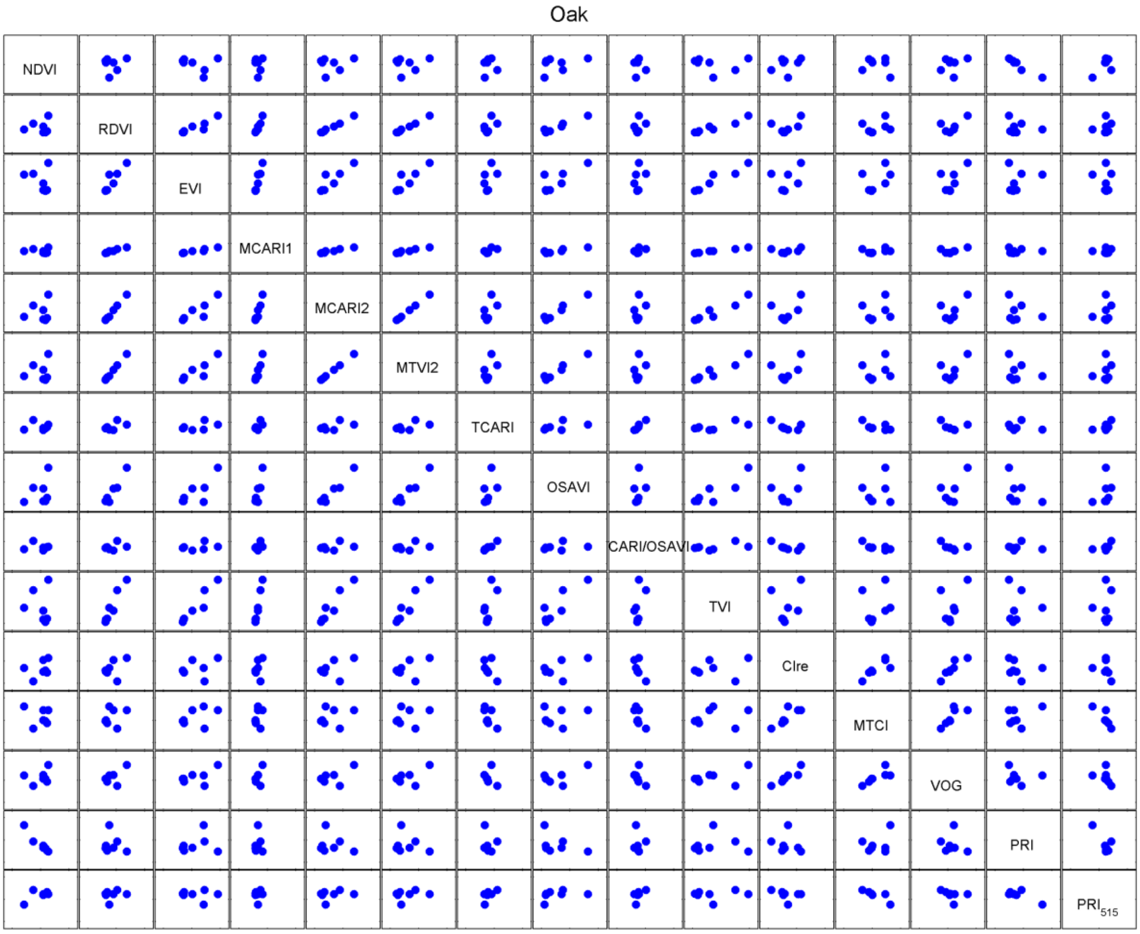

Figure 10. Scatter plots matrix between the different spectral indices obtained from tree pixels reflectance.

Using meteorological data and the optical information extracted from instantaneous and daily averaged GPP and NEE were used to adjust models that predicted carbon fluxes as a function of spectral indices and/or Photosynthetically Active Radiation measured in the EC towers. Models were adjusted using spectral indices corresponding to a) grass pixels, b) trees, c) a mix of both layers weighted by their frequency within the footprint, and d) all the pixels within the footprint.

Table 3 summarizes the regression coefficients of the different models adjusted using spectral indices calculated from grass pixels and instantaneous GPP. In this case, the maximum correlation coefficient (r^2 = 0.85) corresponded to the Model 4 that included the TCARI/OSAVI and the PRI. Similarly, table 4 shows r^2 corresponding to models adjusted using spectral indices of tree pixels. In this case, the maximum coefficient was lower (r^2 = 0.64) and it was found in the Model 5 which mixed OSAVI and PRI_{515}.

Table 3. Correlation coefficient r^2 corresponding to different models that combine grass vegetation indices and instantaneous GPP.

	Model 1	Model 2	Model 3	Model 4	Model 5
NDVI	0.55	0.64	0.63	0.79	0.65
RDVI	0.63	0.60	0.60	0.65	0.59
EVI	0.62	0.56	0.56	0.82	0.57
MCARI1	0.65	0.60	0.57	0.80	0.58
MCARI2	0.63	0.61	0.59	0.82	0.57
MTVI2	0.63	0.61	0.59	0.82	0.57
TCARI	0.57	0.60	0.59	0.84	0.61
OSAVI	0.61	0.62	0.61	0.81	0.62
TCARI/OSAVI	0.49	0.56	0.58	0.85	0.59
TVI	0.64	0.60	0.58	0.64	0.60
CIre	0.67	0.65	0.64	0.74	0.58
MTCI	0.57	0.52	0.53	0.54	0.64
VOG	0.63	0.55	0.61	0.85	0.61

Table 4. Correlation coefficient r^2 corresponding to different models that combine oak vegetation indices and instantaneous GPP.

	Model 1	Model 2	Model 3	Model 4	Model 5
NDVI	0.12	0.45	0.46	0.43	0.64
RDVI	0.09	0.37	0.50	0.50	0.56
EVI	0.00	0.28	0.55	0.51	0.63
MCARI1	0.06	0.30	0.50	0.49	0.56
MCARI2	0.12	0.34	0.49	0.50	0.55
MTVI2	0.12	0.34	0.49	0.50	0.55
TCARI	0.26	0.44	0.49	0.51	0.62
OSAVI	0.14	0.40	0.49	0.35	0.64
TCARI/OSAVI	0.21	0.46	0.51	0.54	0.62
TVI	0.07	0.31	0.48	0.48	0.63
CIre	0.02	0.17	0.56	0.60	0.63
MTCI	0.21	0.07	0.61	0.61	0.62
VOG	0.03	0.36	0.55	0.58	0.63

Eventually, table 5 shows the same results when the models were adjusted using all the pixels in the footprints, including shadows and bare soils. The mix of different covers reduced the maximum r^2 to 0.80 which corresponds to Model 4 using TCARI.

Table 5. Correlation coefficient r^2 corresponding to different models that combine vegetation indices of all the pixels within the footprint and instantaneous GPP.

	Model 1	Model 2	Model 3	Model 4	Model 5
NDVI	0.50	0.62	0.62	0.75	0.63
RDVI	0.66	0.61	0.61	0.79	0.61
EVI	0.64	0.56	0.56	0.60	0.61
MCARI1	0.68	0.61	0.59	0.77	0.61
MCARI2	0.66	0.61	0.60	0.78	0.61
MTVI2	0.66	0.61	0.60	0.78	0.61
TCARI	0.63	0.64	0.63	0.80	0.62
OSAVI	0.63	0.62	0.62	0.79	0.62
TCARI/OSAVI	0.58	0.62	0.66	0.65	0.72
TVI	0.67	0.61	0.59	0.78	0.61
CIre	0.58	0.58	0.58	0.75	0.62
MTCI	0.13	0.39	0.48	0.47	0.61
VOG	0.53	0.52	0.55	0.56	0.61

Conclusions

High spatial resolution airborne imagery has allowed overcoming spatial heterogeneity in a savanna ecosystem, separating optical signals of different covers within the areas of influence of the EC towers.

Multiband radiance-based methods to retrieve SIF have, like FLD and 3FLD have not success to provide reliable estimates. An across-track-related effect has been observed, and we have tried to characterize it. Though we removed the across-track effect, some inconsistencies in the results remained, and at that point the retrieval of reliable SIF estimates was discarded.

Preliminary analysis of a theoretical source of error in the retrieval of SIF* provided some information about the characteristics of the instrumental effect. However, a much deeper study, out of the scope of this STMS, would be needed to properly characterize this phenomenon.

Despite of not being possible include SIF, the flux modeling done is still interesting in the context of the COST Action Optimise, since spatial issues can still be addressed.

Future collaborations with the host institution

Despite of not being able to produce reliable estimates of SIF*, the works started would keep on. On view of the results we have redefined the scientific aims, and we are currently analyzing spatio-temporal issues related with the modelling of carbon fluxes using spectral indices derived from the CASI images. Additional collaborations would take place in frame of field campaigns shared by both groups, Milano Biccoca and SpecLab, in the selected site of this work, Majadas del Tiétar.

Foreseen publications/articles resulting from the STMS

Analysis carried out might lead to results interesting enough to worth a publication. Though some data should still be generated, the analyses are already planned and some trials with preliminary data are promising. We expect to be able to publish the definitive results contributing to a better understanding of the connection between fluxes and high resolution airborne optical data. This work could be of interest in the context of the use UAV in these type of applications, which is one of the issues addressed by the Cost Action OPTIMISE.

Acknowledgements

I would like to thanks the COST Action ES1309 OPTIMISE for supporting this STMS. I would like to especially thank Dr. Micol Rossini for hosting me in the University of Milano-Bicocca. I am very grateful too to all of the colleagues that I met in the Remote Sensing of Environmental Dynamics Laboratory for their interest and the all the feedback and support provided: Mr. Tommaso Julita, Dr. Sergio Cogliati, Dr. Cinzia Panigada, Mr. Marco Celesti, Dr. Roberto Colombo, Mr. Roberto Garzonio, Dr. Francesco Fava, Mr. Biagio di Mauro, Ms. Chiara Cilia and Mr. Fabio Fussi among others. I am very grateful to Dr. Pablo Zarco-Tejada, from IAS-CSIC for the valuable assessment and inputs provided when possible.

I would also like to thank my supervisor Dr. Pilar Martín and to Ms. Pilar Echavarría from SpecLab and to the INTA personnel Mr. Eduardo de Miguel and Ms. Laura Carretero. Thanks also to Dr. Arnaud Carrara and Dr. Cristina Gimeno from CEAM and Dr. Mirco Migliavacca and Mr. Tarek El-Madani from the Max Plank Institute for their help with the eddy covariance data and analyses.

Appendix I. Inclusion of spurious radiance in the Maier equations

From (Maier et al. 2002) we can define the radiance measured by a sensor inside (L_i) and outside (L_o) an atmospheric dark line as follows:

$$\begin{cases} L_i = \left(\rho_i E_i + L_i^f\right) T_i + L_i^p + L_i^s \\ L_o = \left(\rho_o E_o + L_o^f\right) T_o + L_o^p + L_o^s \end{cases} \tag{A1}$$

where i stands for inside the absorption feature and o for outside, ρ is the reflectance factor, E is the irradiance, L^f is radiance emission of fluorescence, T is the transmittance, L^p is the path radiance and L^s is the spurious radiance, a variable that summarize any source of well of radiance due to instrumental effects or others. L^s can be positive or negative, and does not need to be known.

If we assume that $\rho_i = \rho_o = \rho$ and that $L^f{}_i = L^f{}_o = L^f$ then we can deduce that:

$$\begin{cases} \rho = \dfrac{1}{E_i}\left(\dfrac{L_i - L_i^p - L_i^s}{T_i} - L^f\right) = \dfrac{1}{E_o}\left(\dfrac{L_o - L_o^p - L_o^s}{T_o} - L^f\right) \\ L^f = \dfrac{L_i - L_i^p - L_i^s}{T_i} - \rho E_i = \dfrac{L_o - L_o^p - L_o^s}{T_o} - \rho E_o \end{cases} \quad \text{(A2)}$$

Substituting L^f or ρ in A2:

$$L^f = \frac{L_i - L_i^p - L_i^s}{T_i} - \frac{1}{E_o}\left(\frac{L_o - L_o^p - L_o^s}{T_o} - L^f\right)E_i \quad \text{(A3)}$$

$$L^f T_i\left(1 - \frac{E_i}{E_o}\right) = L_i - k_1 L_o - \left(L_i^p - k_1 L_o^p\right) - \left(L_i^s - k_1 L_o^s\right) \quad \text{(A4)}$$

$$L^f k_3 = L_i - k_1 L_o - k_2 - k_s = L_i - k_1{}^* L_o - k_2{}^* \quad \text{(A5)}$$

where k_1^* and k_2^* would be the coefficients eventually adjusted using radiances from non-fluorescent targets and k_2^* is

$$k_2{}^* = k_2 + k_s \quad \text{(A6)}$$

and k_s represents an offset introduced by the spurious radiance, in fact it, as can be deduced from (A5), k_s linearly depends on L^s similarly as k_2 depends on L^p:

$$k_s = L^s{}_i - L^s{}_o\, k_1 \quad \text{(A7)}$$

References

Baldocchi, D.D. (2003). Assessing the eddy covariance technique for evaluating carbon dioxide exchange rates of ecosystems: past, present and future. Global Change Biology, 9, 479-492

Gamon, J.A., Peñuelas, J., & Field, C.B. (1992). A narrow-waveband spectral index that tracks diurnal changes in photosynthetic efficiency. Remote Sensing of Environment, 41, 35-44

Gamon, J.A., Rahman, A.F., Dungan, J.L., Schildhauer, M., & Huemmrich, K.F. (2006). Spectral Network (SpecNet)—What is it and why do we need it? Remote Sensing of Environment, 103, 227-235

Hernández-Clemente, R., Navarro-Cerrillo, R.M., Suárez, L., Morales, F., & Zarco-Tejada, P.J. (2011). Assessing structural effects on PRI for stress detection in conifer forests. Remote Sensing of Environment, 115, 2360-2375

Maier, S.W., Günther, K.P., & Stellmes, M. (2002). Remote sensing and modelling of solarinduced fluorescence. In, 1st Workshop on Remote Sensing of Solar InducedVegetation Fluorescence. ESTEC, Noordwijk, The Netherlands.

Meroni, M., Busetto, L., Guanter, L., Cogliati, S., Crosta, G.F., Migliavacca, M., Panigada, C., Rossini, M., & Colombo, R. (2010). Characterization of fine resolution field spectrometers using solar Fraunhofer lines and atmospheric absorption features. Applied Optics, 49, 2858-2871

Meroni, M., Rossini, M., Guanter, L., Alonso, L., Rascher, U., Colombo, R., & Moreno, J. (2009). Remote sensing of solar-induced chlorophyll fluorescence: Review of methods and applications. Remote Sensing of Environment, 113, 2037-2051

Panigada, C., Rossini, M., Meroni, M., Cilia, C., Busetto, L., Amaducci, S., Boschetti, M., Cogliati, S., Picchi, V., Pinto, F., Marchesi, A., & Colombo, R. (2014). Fluorescence, PRI and canopy temperature for water stress detection in cereal crops. International Journal of Applied Earth Observation and Geoinformation, 30, 167-178

Richards, J.A. (1999). Remote Sensing Digital Image Analysis Berlin: Springer-Verlag

Rossini, M., Cogliati, S., Meroni, M., Migliavacca, M., Galvagno, M., Busetto, L., Cremonese, E., Julitta, T., Siniscalco, C., Morra di Cella, U., & Colombo, R. (2012). Remote sensing-based estimation of gross primary production in a subalpine grassland. Biogeosciences, 9, 2565-2584

Rossini, M., Meroni, M., Migliavacca, M., Manca, G., Cogliati, S., Busetto, L., Picchi, V., Cescatti, A., Seufert, G., & Colombo, R. (2010). High resolution field spectroscopy measurements for estimating gross ecosystem production in a rice field. Agricultural and Forest Meteorology, 150, 1283-1296